materials

Article

# Preparation and Performance of Micro-Arc Oxidation Coatings for Corrosion Protection of $LaFe_{11.6}Si_{1.4}$ Alloy

**Ruzhao Chen [1,2], Bin Fu [1,2], Jie Han [3,*], Hu Zhang [4,*], Ping Wang [5] and Hongxia Yin [5]**

[1] School of Material Science and Engineering, Tianjin University of Technology, Tianjin 300384, China; chenruzhao2020@126.com (R.C.); fubin@tjut.edu.cn (B.F.)
[2] Key Laboratory of Display Materials and Photoelectric Devices, Ministry of Education, Tianjin University of Technology, Tianjin 300384, China
[3] College of Science, Tianjin University of Technology, Tianjin 300384, China
[4] School of Materials Science and Engineering, University of Science and Technology Beijing, Beijing 100083, China
[5] School of Material Science and Engineering, Yantai Nanshan University, Yantai 265713, China; wangping87881904@163.com (P.W.); yinhongxia_816@163.com (H.Y.)
* Correspondence: hanjie@email.tjut.edu.cn (J.H.); zhanghu@ustb.edu.cn (H.Z.)

**Abstract:** The microstructure, corrosion resistance, and phase-transition process of micro-arc oxidation (MAO) coatings prepared on $LaFe_{11.6}Si_{1.4}$ alloy surfaces in different electrolyte systems were systematically investigated. Research has demonstrated that various electrolyte systems do not alter the main components of the coatings. However, the synergistic action of $Na_2CO_3$ and $Na_2B_4O_7$ more effectively modulated the ionization and chemical reactions of the MAO process and accelerated the formation of $\alpha$-$Al_2O_3$. Moreover, the addition of $Na_2CO_3$ and $Na_2B_4O_7$ improved the micromorphology of the coating, resulting in a uniform coating thickness and good bonding with the $LaFe_{11.6}Si_{1.4}$ substrate. The dynamic potential polarization analysis was performed in a three-electrode system consisting of a $LaFe_{11.6}Si_{1.4}$ working electrode, a saturated calomel reference electrode, and a platinum auxiliary electrode. The results showed that the self-corrosion potential of the $LaFe_{11.6}Si_{1.4}$ alloy without surface treatment was −0.68 V, with a current density of $8.96 \times 10^{-6}$ A/cm$^2$. In contrast, the presence of a micro-arc electrolytic oxidation coating significantly improved the corrosion resistance of the $LaFe_{11.6}Si_{1.4}$ substrate, where the minimum corrosion current density was $1.32 \times 10^{-7}$ A/cm$^2$ and the corrosion potential was −0.50 V. Similarly, after optimizing the MAO electrolyte with $Na_2CO_3$ and $Na_2B_4O_7$, the corrosion resistance of the material further improved. Simultaneously, the effect of the coatings on the order of the phase transition, latent heat, and temperature is negligible. Therefore, micro-arc oxidation technology based on the in situ growth coating of the material surface effectively improves the working life and stability of La(Fe, Si)$_{13}$ materials in the refrigeration cycle, which is an excellent alternative as a protection technology to promote the practical process of magnetic refrigeration technology.

**Keywords:** La-Fe-Si alloys; magnetic refrigeration materials; micro-arc oxidation; microstructure; corrosion resistance

**Citation:** Chen, R.; Fu, B.; Han, J.; Zhang, H.; Wang, P.; Yin, H. Preparation and Performance of Micro-Arc Oxidation Coatings for Corrosion Protection of $LaFe_{11.6}Si_{1.4}$ Alloy. *Materials* **2024**, *17*, 1316. https://doi.org/10.3390/ma17061316

Academic Editor: Konstantin Borodianskiy

Received: 20 February 2024
Revised: 9 March 2024
Accepted: 11 March 2024
Published: 13 March 2024

## 1. Introduction

Magnetic cooling technology is based on the magnetocaloric effect (MCE) [1,2], which refers to the magnetic entropy change ($\Delta S_M$) or temperature change ($\Delta T_{ad}$) produced by the application or removal of a magnetic field in adiabatic (or isothermal) conditions [3]. Compared to conventional cooling technology, it is highly efficient, environmentally friendly, stable, and reliable. Therefore, it is a novel and highly promising refrigeration technology. As the core of magnetic refrigeration technology, research regarding magnetic refrigeration working media is critical. Thus far, magnetocaloric materials with large MCEs near room temperature, such as $Gd_5Si_{4-x}Ge_x$ [4], La(Fe, Si)$_{13}$ [5], and $MnFeP_xAs_{1-x}$-based compounds [6], as well as certain rare earth-based oxides, alloys, and microwires [7], have been explored. Among these, La(Fe, Si)$_{13}$-based materials with $NaZn_{13}$ crystals are considered one of the most feasible alternative refrigerants for magnetic refrigeration owing to their significant advantages of having large MCEs, relatively high cooling power, and non-toxic constituent elements [8]. In addition, La(Fe, Si)$_{13}$-based compounds have adjustable Curie temperatures ($T_C$). However, as a typical first-order phase-transition MCE material, the order of the magnetic phase transition of La(Fe, Si)$_{13}$ has a strong relationship with the Si content [9]. When $1.2 \leq x \leq 1.6$, $LaFe_{13\text{-}x}Si_x$ compounds demonstrate intense magnetically elastic coupling characterized by a lager negative expansion of the lattice at the Curie temperature and a magnetic-field-induced itinerant-electron metamagnetic transition (IEMT) [10]. Concurrently, the large changes in the magnetization and lattice parameters near the Curie temperature cause the La(Fe, Si)$_{13}$ series of compounds to present significant magnetocaloric properties, and a small change in the magnetic entropy versus temperature curve [11].

Heat exchange is an important component in the working process of a magnetic refrigerator. Owing to their large heat capacity and high thermal conductivity, aqueous solutions or water-based fluids are utilized as highly efficient heat-exchange media between the magnetic refrigerants and loads for magnetic refrigerators operating near room temperature [12]. Notedly, $LaFe_{13-x}Si_x$ compounds severely corrode in water without protection, which not only diminishes the working efficiency of the refrigerator but also damages its stability and working life [13]. In many cases, corrosion degradation deteriorates the magnetocaloric effect of the material, and the corrosion products affect the fluidity and heat conduction of the heat-transfer medium. Therefore, corrosion protection must be considered in practical processes. The causes of La(Fe, Si)$_{13}$ material corrosion were investigated considering two perspectives. On the one hand, they contain the highly chemically active rare-earth element La, and on the other hand, the multi-phase structure and high potential difference between the phases caused by the non-equilibrium solidification of the La(Fe, Si)$_{13}$ material weakens the electrochemical corrosion of the magnet when contacting the heat-exchange fluid [14]. The corrosion mechanism of the La(Fe, Si)$_{13}$-based alloy principally depends on its multi-phase structure, and a micro galvanic couple is formed between two adjacent phases to accelerate the corrosion rate [15].

Thus far, several theoretical studies regarding corrosion behavior have been conducted considering the constituent elements, chemical composition, and original microstructure. By studying the corrosion resistance of annealed $LaFe_{11.6}Si_{1.4}B_y$ series alloys, $Fe_2B$ was found to replace $\alpha$-Fe in the second phase after B doping, the difference in the micro galvanic corrosion potential between the second and matrix phases decreased, as well as the mixed current density, which inhibited the corrosion of the main phase [16]. Similarly, research regarding the latent heat behavior of La(Fe, Mn, Si)$_{13}$ in the thermal cycle has demonstrated that Mn-doping can reduce the corrosion potential difference and strengthen the corrosion resistance of the alloy [17]. Additionally, the effect of adding Co and C was investigated, which concluded that the addition of Co and C can significantly enhance the membrane impedance and promote the formation of a protective corrosion membrane layer [14]. In addition, the non-stoichiometric La(Fe, Si)$_{13}$ base alloy can also improve the corrosion resistance [18] by increasing the content of the specific impurity phases to amplify the magnetic and corrosion properties of the alloys.

In addition to the composition and inherent structural improvements, a utilization strategy for magnetocaloric materials coated with corrosion-resistant materials in refrigeration units was proposed, which inspired another study that revealed the corrosion behavior of $LaFe_{11.5}Si_{1.5}$/Cu compounds and found that Cu cladding separates the magnetic refrigeration working medium and corrosion liquid, effectively heightening the corrosion potential, reducing the corrosion current density, and improving the corrosion resistance of the alloy [19]. However, to ensure an efficient heat exchange with the heat-transfer liquid in AMR cycles, the materials must be processed into large surface areas. The application of cladding materials remains difficult, owing to several issues such as being limited to simple molded parts, poor cladding tightness, and the plating-liquid contamination of the environment [20]. The ion-implantation technology is not dependent on the silhouette. By using Cu ion implantation in the $LaFe_{11.6}Si_{1.4}$ alloy, the results indicated that the corrosion potential increased and the corrosion current decreased with Cu-ion implantation in the $LaFe_{11.6}Si_{1.4}$ alloy [21]. Nevertheless, the copper-formed surface corrosion layer is not as dense as those of other metal oxides, resulting in uneven and loose phenomena that accelerate corrosion. Recently, micro-arc oxidation (MAO) technology has been widely used in the anti-corrosion process of medical magnesium–zinc alloys owing to their dense and uniform coating, which has a good anti-corrosion performance, simple operation, no pollution, and no strict requirements for the appearance of the matrix materials [22]. At present, micro-arc oxidation technology is mainly applied to metals such as Mg, Al, and Ti, rather than Fe-based alloys. The main reason is that the MAO coating directly formed on the Fe substrate is not stable enough to achieve good corrosion resistance. In the trial experiment of the micro-arc oxidation of an iron-based rare-earth $La(Fe, Si)_{13}$ alloy, it was found that the addition of rare-earth elements significantly improved the performance of MAO coatings on this series of alloys. If suitable electrolytes can be used, it is expected to obtain MAO coatings with good corrosion resistance. Therefore, the study of $La(Fe, Si)_{13}$ series alloy MAO coatings is not only beneficial for the practical application of magnetic refrigeration technology, but also can promote the application of this coating on Fe-based alloys. However, there are no current studies regarding them.

In this study, a $LaFe_{11.6}Si_{1.4}$ alloy was used as the substrate of micro-arc oxidation. According to previous studies, the main component of the aluminate electrolyte system is $Al_2O_3$, which has a high strength, hardness, and abrasiveness, whereas the coating formed by it is compact and uniform, has a good thermal conductivity, and high corrosion resistance. Therefore, three electrolyte solutions based on the aluminate electrolyte system were designed using $NaAlO_2$, $Na_2CO_3$, $NaH_2PO_4$, and $Na_2B_4O_7$. The micro morphology of the MAO coating and its influence on the corrosion resistance and phase-transition process of $LaFe_{11.6}Si_{1.4}$ materials were systematically studied. This study introduces the foundation for preparing in situ MAO metal coatings on the surfaces of $La(Fe, Si)_{13}$ magnetothermal materials.

## 2. Experimental

$LaFe_{11.6}Si_{1.4}$ alloys were prepared by arc-melting pure La (99.9%), Fe (99.9%), and Si (99.9%) in a high-purity argon atmosphere. Cylinder samples of $\Phi 8 \times 3$ ($\pm 0.1$) mm in size were cut out of the ingot. The samples were annealed at 1323 K for 12 days in a quartz tube filled with an argon atmosphere, followed by ice-water quenching. The oxides on the surface of the sample were removed using a 1000-mesh silicon carbide sandpaper. Surface grease was then removed by ultrasonic cleaning. In the MAO process, the $LaFe_{11.6}Si_{1.4}$ sample was the working anode and the stainless steel was the cathode. The voltage and pulse frequency were set at 500 V and 1200 Hz, respectively, and the treatment duration was 20 min. The electrolyte temperature was maintained at 20 °C by circulating the water-cooling bath. The main electrolytes used for MAO were $NaAlO_2$, $Na_2CO_3$, $NaH_2PO_4$, and $Na_2B_4O_7$. Table 1 and Figure 1 list the combinations of electrolytes and the schematic diagram of the MAO device used in this experiment; the coatings prepared are represented by M1, M2, and M3, respectively.

**Table 1.** Composition and concentration of the electrolytes used in different MAO coatings.

| Coatings | $NaAlO_2$ (g/L) | $NaH_2PO_4$ (g/L) | $Na_2CO_3$ (g/L) | $Na_2B_4O_7$ (g/L) |
|---|---|---|---|---|
| M1 | 15 | 3 | / | / |
| M2 | 15 | 3 | 3 | / |
| M3 | 15 | 3 | 3 | 3 |

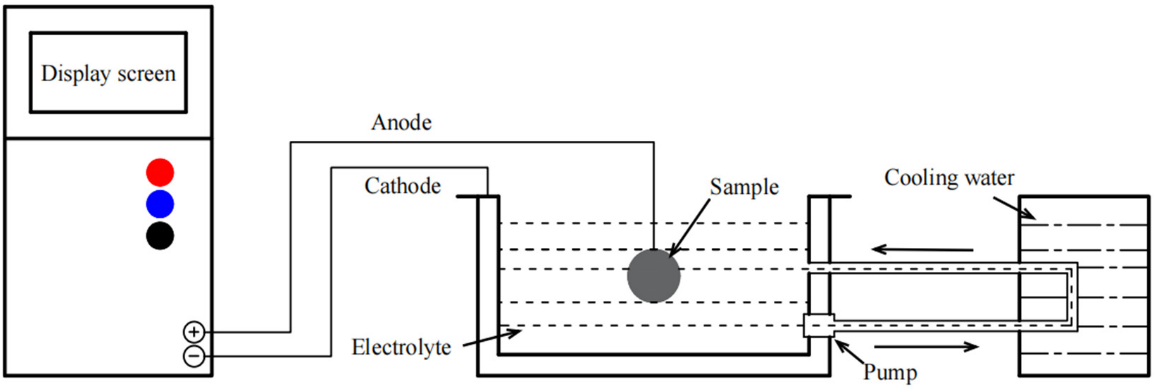

**Figure 1.** Schematic diagram of the micro-arc oxidation device.

The microstructures and elemental compositions of the coatings were analyzed using scanning electron microscopy (SEM, JSM-6360LV, JEOL, Tokyo, Japan) and energy-dispersive spectrometry (EDS, Oxford Atec X-max 50, Oxford Company, Oxford, UK). X-ray diffraction (XRD, Ultima-IV, Rigaku, Tokyo, Japan) was used to study the crystal structure of the samples. The porosity of the coating surface was quantified using ImageJ software (ImageJ 1.8.0, National Institutes of Health, Bethesda, MD, USA). The coating-binding force was tested using a WS-2005 coating adhesion scratch instrument (Shanghai Shenrui Instrument Co.,Ltd., Shanghai, China).

Dynamic polarization (IE) testing of the coatings was performed using a standard three-electrode electrochemical analyzer/workstation (VersaSTAT MC, Ametek Company, Berwyn, PA, USA). For the electrochemical study, each measurement was performed in a standard three-electrode cell consisting of a $LaFe_{11.6}Si_{1.4}$ working electrode, saturated calomel reference electrode (SCE), and platinum counter electrode. Distilled water was used as the test solution in the 0.2 $cm^2$ test area. The polarization curves of the samples in the test solution were recorded at a scanning speed of $1 \times 10^{-3}$ V/s. The thermal cycle was conducted near $T_C$ using differential scanning calorimetry (DSC, DSC214, NETZSCH-Gerätebau GmbH, Selb, Germany) at a scanning rate of 3 K/min.

## 3. Results and Discussion

Figure 2 presents the XRD patterns of the MAO-coated samples with different electrolyte compositions, which demonstrates that all the MAO coatings present characteristic peaks of $\alpha$-$Al_2O_3$, $\gamma$-$Al_2O_3$, $Fe_2O_3$, $FeAl_2O_4$, and $FePO_4$, indicating that different electrolyte compositions did not change the main components of the MAO coatings. Specifically, the diffraction peaks of $Fe_2O_3$ and $FePO_4$ were observed at 45.5° and 65.0° [23], respectively, for all the samples. Notably, owing to the layered porous structure of the coating, X-rays can penetrate the coating onto the $Fe_2O_3$-dense oxide layer, resulting in the appearance of $Fe_2O_3$ diffraction peaks. This also indicates that the iron oxide on the substrate participates in the MAO reaction [23,24]. In addition, the $FeAl_2O_4$ diffraction peak was located at 45.5°, which overlaps with those of the first two Fe-containing compounds [24]. The diffraction peaks of $\alpha$-$Al_2O_3$ were located at 31.7°, 37.2°, 44.6°, 60.3°, and 66.0°, and 43.3°, 47.0°, 56.3°, and 82.5° corresponded to $\gamma$-$Al_2O_3$. Compared with M1, the diffraction-peak intensity of $Fe_2O_3$ remarkably decreased in the M2 spectrum, whereas those of $\alpha$-$Al_2O_3$ and $\gamma$-$Al_2O_3$ increased, indicating that the addition of $Na_2CO_3$ promotes the growth of the $\alpha$-$Al_2O_3$ film layer and affects the reaction of MAO [25,26]. The diffraction peaks of $Fe_2O_3$ and $FePO_4$ in M3 nearly disappeared, and the intensity of the $\gamma$-$Al_2O_3$ diffraction peaks decreased, indicating that the addition of the $Na_2B_4O_7$ resolved the iron-oxide formation and significantly inhibited $FePO_4$ formation in the envelope [27]. Generally, the type of $Al_2O_3$ crystal in the coating directly affects the corrosion resistance, and a higher content of $\alpha$-$Al_2O_3$ improves the corrosion resistance.

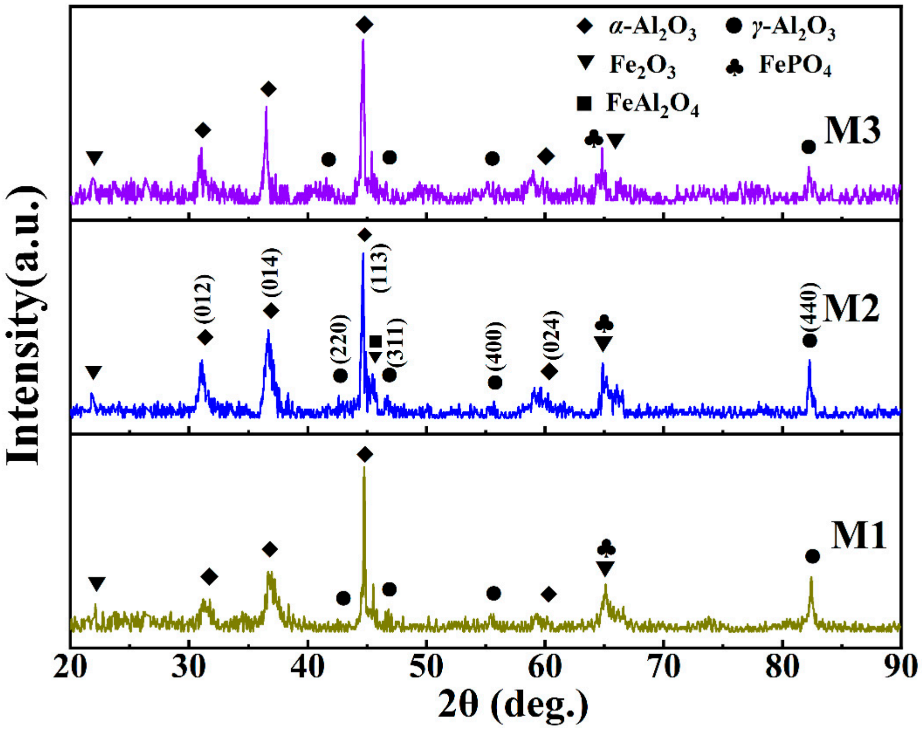

**Figure 2.** XRD pattern of the MAO coating under different electrolyte components.

Figure 3a–d, as well as Figure 3e,f, demonstrate the surface morphology of M1, M2, and M3 MAO coatings prepared under different electrolyte compositions, respectively. The content of each element obtained from the EDS analysis is listed in Table 2. Because it was performed in a constant pressure mode, the sample surfaces under different electrolytes exhibited "volcanic characteristics" of the MAO coating [28,29]. The mastoid morphology is the main surface feature that can be observed in the high magnification images, as shown in point A in Figure 3a, where the upper-right illustration presents an enlarged view of point A. All the coatings have black circular pores distributed in the molten region on the surface. These circular micropores are volcanic vents, which are residual channels of the discharge reaction, and are caused by the outflow of molten oxides from the discharge channel and are cooled by relatively cold electrolytes [30]. The microcracks in the coating are caused by the thermal stress generated by the rapid solidification of molten oxide [31]. The coating of numerous microcracks and microporous structures was clearly observed in M1, resulting in an uneven surface and higher roughness (Figure 3b). However, the appearance of cracks indicates that the formation process of the MAO coating is unstable during arc interruption, and it also suggests the presence of loose $Fe_2O_3$ and $FePO_4$. Similarly, the pores and cracks as defects will be detrimental to the anti-corrosion performance of the material. M1 is mainly composed of Al, O, Fe, and P elements, with Al and Fe atoms accounting for 29.7% and 6.6%, respectively, as shown in Table 2. When $Na_2CO_3$ was added to M2, the small hole at the center of the circular surface protrusion was a typical charge perforation in the MAO process (Figure 3d). $Na_2CO_3$ has a positive impact on the formation of coatings, which is manifested by a significant reduction in the surface cracks, a lower roughness, and a denser coating. This phenomenon is due to the addition of $Na_2CO_3$, changing the solution environment and thus improving the discharge mechanism [25,26], making it more conducive to the production of $Al_2O_3$, resulting in a higher content of $Al_2O_3$ in the coating. The EDS analysis confirms that the content of Al and O slightly increased in M2, whereas the content of Fe and P decreased, indicating that the growth of the $Al_2O_3$ crystals effectively improved during the MAO process [32]. The surface morphology of M3 is generally consistent with that of M2, but the large pores are significantly reduced, shrinking to half. The coating surface is uniform and dense (Figure 3e). During the formation process of M3 coating, the addition of $Na_2CO_3$ and $Na_2B_4O_7$ further improved the discharge mechanism of micro-arc oxidation [28], thereby changing the formation mechanism of the surface layer and leading to the disappearance of cracks and the sealing of most discharge holes. On the other hand, the presence of $Na_2B_4O_7$ promoted the decomposition of iron oxide, making it more conducive to the generation of $Al_2O_3$. Therefore, the combined effect resulted in a smoother and more uniform surface layer of the M3 coating. According to the EDS results, the atomic percentages of Al and O are 36.9% and 58.2%, respectively, with a ratio of 0.634, which is notably close to the Al/O ratio of the $Al_2O_3$ compound (0.667). Overall, the addition of both $Na_2B_4O_7$ and $Na_2CO_3$ regulates the reaction process, significantly inhibiting the oxidation reaction of Fe in the substrate and catalyzing the generation of $Al_2O_3$. Simultaneously, the appropriate amount of $Na_2CO_3$ or $Na_2B_4O_7$ makes the coating surface uniform and delicate.

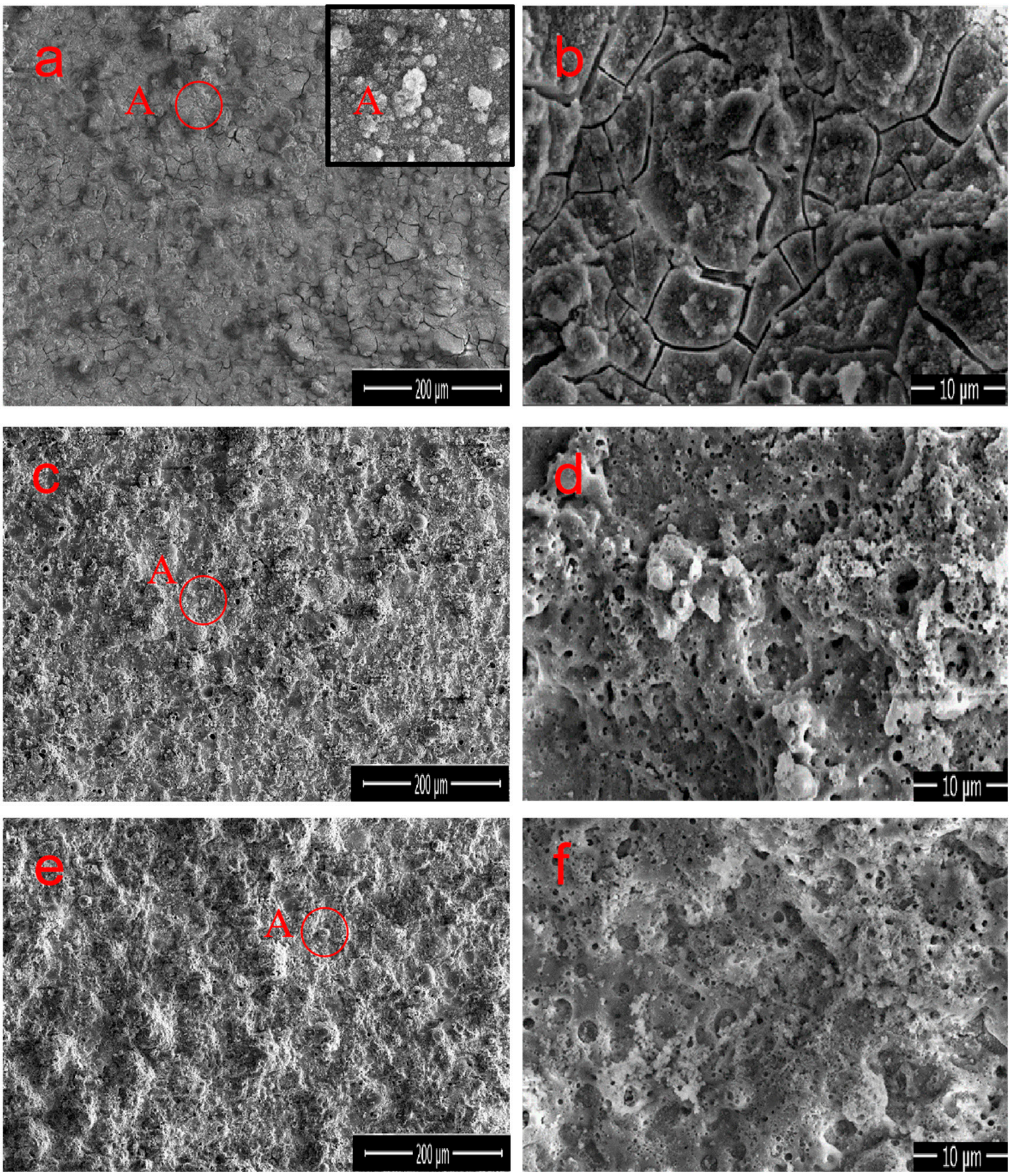

**Figure 3.** SEM images of the (**a**,**b**) M1, (**c**,**d**) M2, and (**e**,**f**) M3 MAO coatings under different electrolyte compositions. The right images correspond to enlarged views of area A in the left images.

**Table 2.** The elemental content (atomic percentage) of the MAO coatings under different electrolyte components.

| Sample | Al (%) | O (%) | P (%) | Fe (%) |
|---|---|---|---|---|
| M1 | 29.7 | 59.9 | 3.9 | 6.6 |
| M2 | 33 | 60.4 | 3.1 | 3.6 |
| M3 | 36.9 | 58.2 | 2.3 | 2.7 |

The cross-sectional SEM morphologies and EDS elemental line-scanning distribution curves of the MAO coatings in different electrolytes are shown in Figure 4. Figure 4a,c,e correspond to M1, M2, and M3, respectively. Specifically, Figure 4b,d,f correspond to the enlarged views of the region in the circle in Figure 4a,c,e, respectively, whereas a1, b2, and c3 correspond to the line scanning at the transverse line, respectively. Figure 4a demonstrates that the coating thickness is uniform, whereas Figure 4b indicates that the substrate material is closely connected to the coating; however, the presence of deeper cracks causes the coating surface to become dense and thus fall off. In addition, the line-scan pattern demonstrates that the diffraction peaks of Al and O are alternately serrated, whereas the diffraction peaks of Fe and P appear simultaneously. This indicates that the compositional distribution of the coating was uneven and that there were other oxides that significantly reduced the bonding strength. Furthermore, the average coating thickness of M1 was 40 ± 2 μm. The overall condition of M2 was good, but according to the energy spectrum, impurities remained and the coating thickness (33 ± 2 μm) was smaller than the other two coatings. The coating thickness of M3 reached 65 ± 2 μm, there was no gap with the substrate, and its cross-sectional state was sufficiently stable, dense, and smooth. A comparison of the thicknesses of the coatings is shown in the SEM images. Changes in the electrolyte composition can apparently result in significant differences in the cross-sectional morphologies of the coatings. Notedly, there was a stable Fe-A1 co-position transition zone between the coating and substrate with a thickness of 3 ± 0.5 μm, indicating that substrate oxidation occurs during the initial stage of the coating formation.

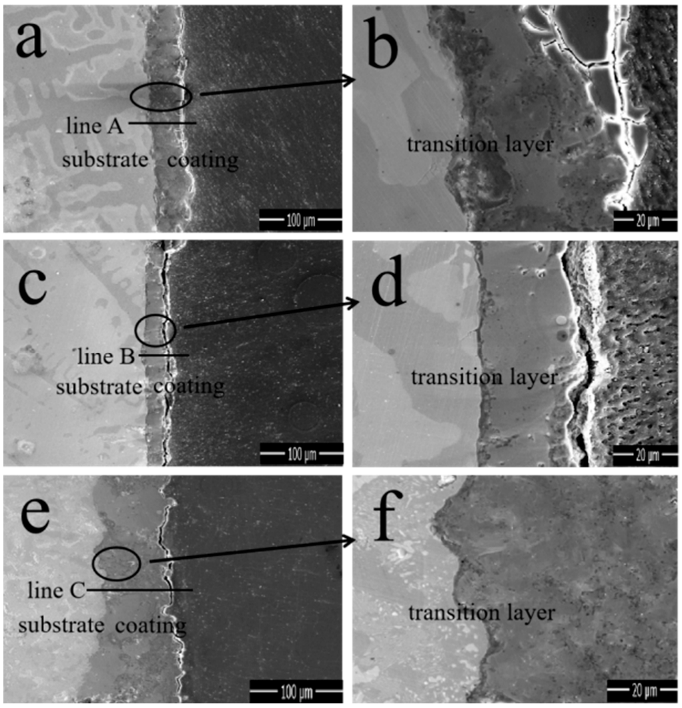

**Figure 4.** *Cont.*

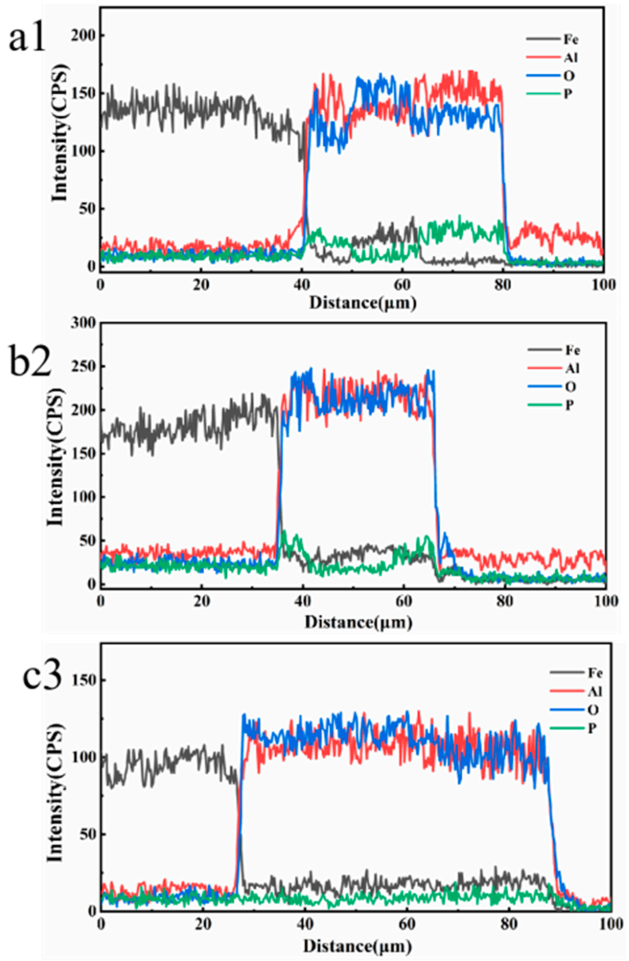

**Figure 4.** SEM image and EDS line-scan distribution curve of the MAO coating cross-section: (**a**,**b**,**a1**) M1, (**c**,**d**,**b2**) M2, (**e**,**f**,**c3**) M3.

The surface pore distribution of the MAO coatings with different electrolytes is shown in Figure 5a–c, where a–c corresponds to M1–M3, respectively, and the porosity calculated using the ImageJ software is shown in Figure 5d. Overall, owing to the constant pressure mode, the dominant pore structure was the discharge channel [33]. M1 was mainly composed of micropores and cracks with a porosity of 15.28%. The addition of $Na_2CO_3$ to M2 significantly regulated the MAO-discharge process and improved the density of the membrane layer and growth of the outer layer, resulting in the formation of a porous morphology; its porosity decreased to 10.78%. When $Na_2B_4O_7$ was added, the porosity did not change; however, the hole diameter significantly decreased. This is because the discharge process significantly improved, the conductivity was enhanced, and the solidified oxide melted and decomposed again, causing it to slightly solidify or become submerged when encountering colder electrolytes. In conclusion, an appropriate electrolyte composition can improve the pore morphology of the coating surface and make it smooth, compact, and uniform.

The bonding strength between the coatings and the La-Fe-Si substrate is critical for practical use. In this regard, Figure 6 presents the bonding-force analysis of the coatings prepared with different electrolyte components. According to this definition [34], the peak position of the first acoustic signal corresponds to the load capacity, that is, the bonding force. The ratio of the first load to the surface area of the sample is the bonding strength. Figure 6 demonstrates that M1 had the lowest adhesion among the three coatings, for which the bonding force was 10.83 ± 0.15 N and bonding strength was 86.25 ± 1.18 MPa. This is owing to the crack defects, an unstable Fe-Al transition layer, and a complex coating composition, resulting in a low bonding force. The bonding force of M2 was 16.65 ± 0.37 N, and the bonding strength was 132.56 ± 2.29 MPa. Compared with M1, the bonding capacity of M2 increased, which further verifies that the addition of $Na_2CO_3$ changes the discharge reaction and improves the distribution of the coating structure and diffusion process of the components. However, the bonding force and bonding strength of the M3 coating slightly decreased, which were 16.05 ± 0.44 N and 127.80 ± 3.54 MPa, respectively. This is owing to the influence of the discharge reaction on the M3 layer; furthermore, the increase in pores in the outermost membrane layer leads to a decrease in the density, and the stability of the Fe-A1 transition layer remains unchanged.

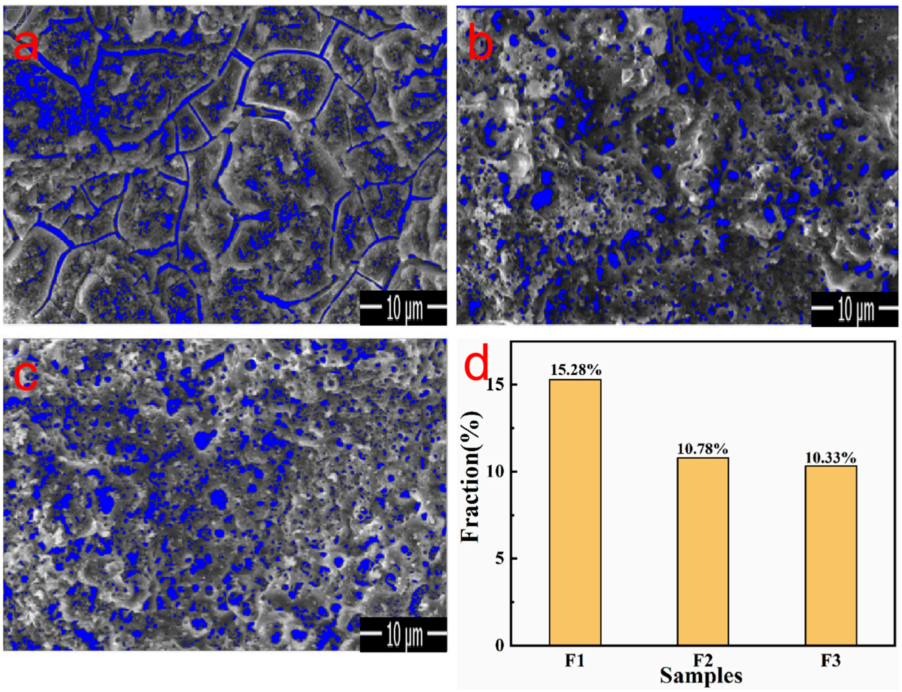

**Figure 5.** Pore images of the MAO coatings under different electrolyte components (**a**–**c**); porosity bar chart (**d**).

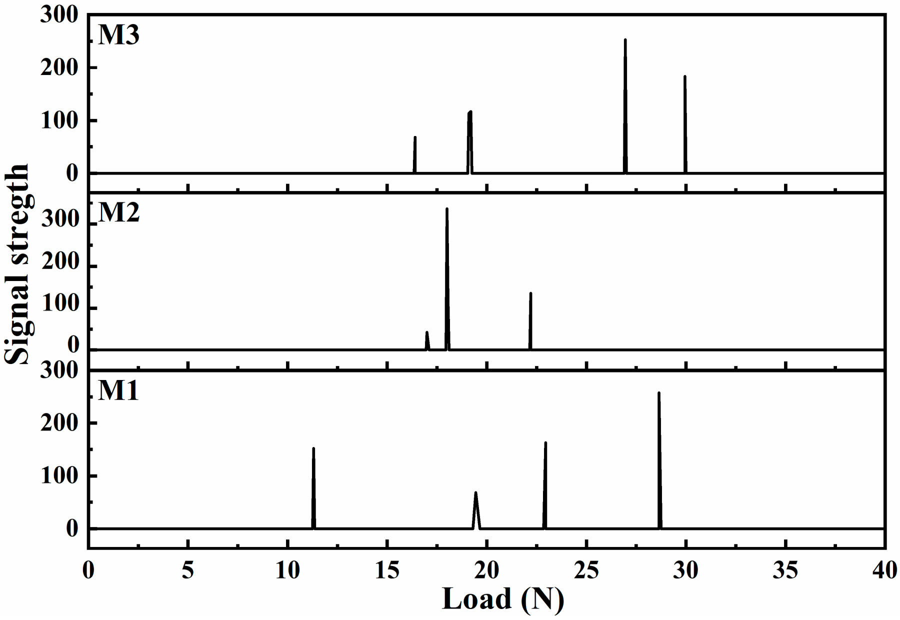

**Figure 6.** Adhesion of the MAO coatings under different electrolyte compositions.

Figure 7 presents the polarization curves (PDP) obtained from the kinetic potential polarization tests of the samples prepared in different electrolytes in distilled water. The dynamic potential polarization analysis was performed in a three-electrode system consisting of a $LaFe_{11.6}Si_{1.4}$ working electrode, a saturated calomel reference electrode and a platinum auxiliary electrode. The electrochemical data obtained after Tafel fitting are shown in Table 3. The samples without coatings demonstrated poor corrosion resistance, whereas those with coatings had significantly improved corrosion resistance. Among these, the M3 coating exhibited the best protective performance, with a polarization potential and corrosion current density of $-0.50$ V and $1.32 \times 10^{-7}$ $A/cm^2$, respectively, which was owing to the large coating thickness and small pore size, inhibiting the corrosion of the sample. The corrosion potential apparently increased from $-0.68$ V of $LaFe_{11.6}Si_{1.4}$ to $-0.50$ V of M3, and the corrosion current density decreased from $8.96 \times 10^{-6}$ $A/cm^2$ to $1.32 \times 10^{-7}$ $A/cm^2$, indicating an increase in the corrosion potential and decrease in the corrosion current density of the sample. This also confirms that the addition of $Na_2CO_3$ and $Na_2B_4O_7$ improved the microstructure of the coating and enhanced the corrosion resistance of the substrate material.

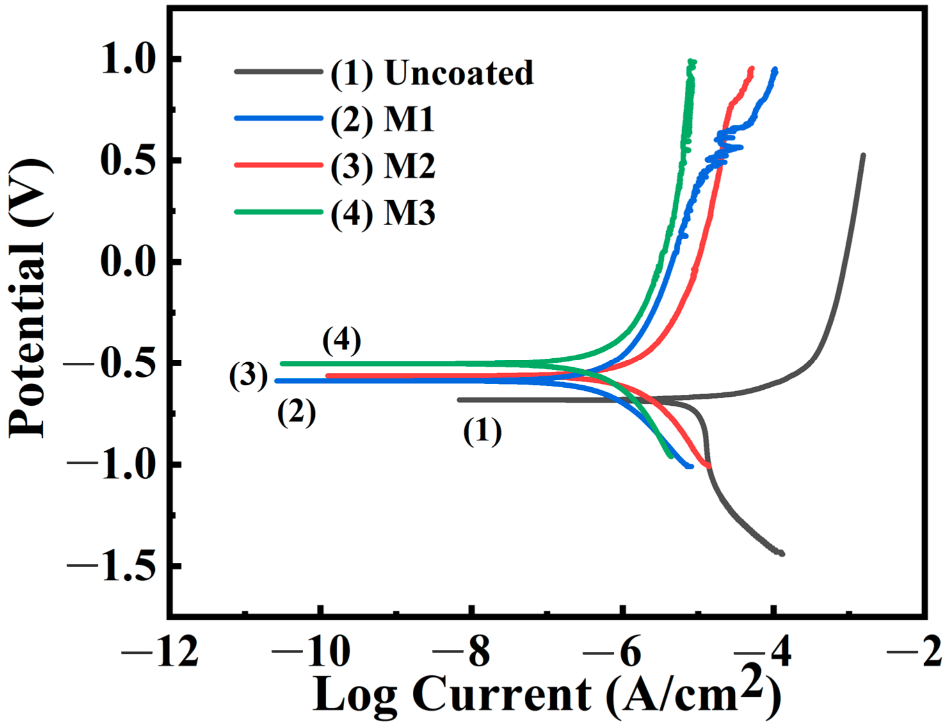

**Figure 7.** Polarization curves of the MAO coatings under different electrolyte compositions.

**Table 3.** MAO coating data fitted by the Tafel polarization curve under different electrolyte compositions.

| Sample | Corrosion Current Density $i_{corr}$ ($A/cm^2$) | Corrosion Potential $E_{corr}$ (V) | Corrosion Rate CR (mm/y) |
|---|---|---|---|
| $LaFe_{11.6}Si_{1.4}$ | $8.96 \times 10^{-6}$ | $-0.68$ | 0.0690 |
| M1 | $3.37 \times 10^{-7}$ | $-0.56$ | 0.0026 |
| M2 | $1.51 \times 10^{-7}$ | $-0.53$ | 0.0011 |
| M3 | $1.32 \times 10^{-7}$ | $-0.50$ | 0.0010 |

The aforementioned results were obtained owing to the following: ① The coating has a higher $\alpha$-$Al_2O_3$ content, and its good coating performance separates the substrate from the solution, inhibits the corrosion of the substrate, and decelerates the electrochemical corrosion. ② Owing to the unique, uniform, and dense micromorphology of the constant-voltage discharge mode, contact with the heat-exchange medium is effectively avoided.

③ Owing to the high bonding strength of the coating, the dense layer and substrate were directly connected.

As indicated above, the coating was successfully prepared on the surface of the $LaFe_{11.6}Si_{1.4}$ alloy, and the corrosion resistance of the substrate was effectively improved. Owing to the need for heat exchange between the magnetic refrigeration materials and the medium during the operation, it is necessary to consider whether the coating affects the heat absorption and release during the phase-transition process. The M3 coating demonstrated an excellent corrosion resistance, as shown in Figure 8, which presents the DSC curves of the samples without the surface treatment and M3-coated samples; here, the peak represents the heat absorbed by the material during the phase-transition process. The phase-transition temperatures, determined by differentiating the DSC (DDSC) curves [35], were 190 K and 187 K, respectively. Endothermic peaks occurred at the same temperature during the thermal cycling process, indicating that the phase transition temperature was nearly consistent during the cycling process [36,37]. The phase-transition latent heat indicates the integral of the DSC curve peak over time [38]:

$$\Delta H = \int \frac{dQ}{dt} \cdot dt \tag{1}$$

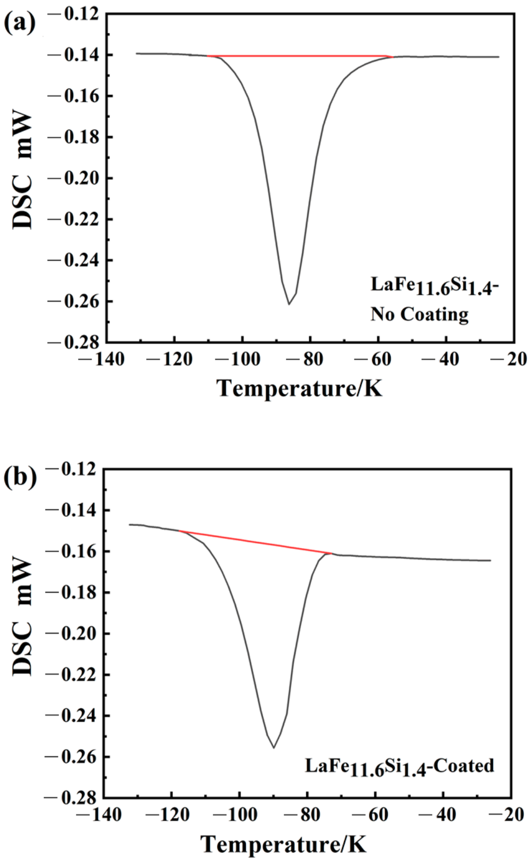

**Figure 8.** DSC curves of the $LaFe_{11.6}Si_{1.4}$ compound (**a**) without coating and (**b**) with coating.

In the formula, $\frac{dQ}{dt}$ is the heat-flux rate, expressed as the difference in power delivered to the sample and the reference while keeping their temperatures equal (where $Q$ and $t$ are heat and time, respectively). The $\int \frac{dQ}{dt} \cdot dt$ is the latent heat, which is directly calculated by the built-in software of the DSC equipment (NETZSCH Proteus 5.0, NETZSCH-Gerätebau GmbH, Selb, Germany). The calculations determined that the values without and with the coating were 4.43 J/g and 4.26 J/g, respectively. The phase-change latent heats of the uncoated and coated samples were nearly identical. In addition, the sharp latent thermal peak indicates that the coated $LaFe_{11.6}Si_{1.4}$ remains a first-order magnetic-phase transition material. Therefore, the micro-arc oxidation technology not only improves the corrosion resistance of the material, but also does not alter the other properties, which is critical for protecting the substrate from damage.

## 4. Conclusions

In this study, the micromorphology, coating performance, corrosion resistance, and magnetocaloric effect of MAO coatings prepared on $LaFe_{11.6}Si_{1.4}$ alloy surfaces using different electrolyte systems were systematically compared and analyzed. X-ray diffraction mapping revealed that the different electrolyte systems had little effect on the main components of the coating; however, there were apparent differences in the $Al_2O_3$ content. The addition of $Na_2CO_3$ and $Na_2B_4O_7$ significantly improved the MAO-discharge process, making the coating structure and morphology on the $LaFe_{11.6}Si_{1.4}$ alloy surface more compact and smoother, with a more uniform thickness and improved performance. Furthermore, the addition of $Na_2CO_3$ and $Na_2B_4O_7$ reduced the surface porosity and pore diameter of the $LaFe_{11.6}Si_{1.4}$ alloy while improving the binding force and binding strength between the coating and substrate, which were $16.65 \pm 0.37$ N and $132.56 \pm 2.29$ MPa, respectively. Compared with the alloy without the surface treatment, the corrosion resistance of the $LaFe_{11.6}Si_{1.4}$ alloy with the MAO coating was significantly improved, and the self-corrosion current density of the coating was reduced to $1.32 \times 10^{-7}$ A/cm$^2$. In addition, the MAO coating enhanced the corrosion resistance without affecting the magnetothermal properties of the $LaFe_{11.6}Si_{1.4}$. Therefore, micro-arc oxidation, a technology that decelerates the corrosion of the substrate, effectively provides corrosion protection for $La(Fe, Si)_{13}$ in refrigeration cycles and is expected to promote the practicality of magnetic refrigeration technology.

**Author Contributions:** Conceptualization, B.F.; Methodology, J.H.; Validation, H.Z.; Investigation, R.C.; Resources, H.Y.; Data curation, P.W.; Writing—original draft, R.C. and B.F.; Writing—review & editing, H.Z.; Supervision, J.H. All authors have read and agreed to the published version of the manuscript.

**Funding:** This work was supported by the Longkou City Science and Technology Research and Development Plan Project (Grant No.: 2021KJJH025).

**Institutional Review Board Statement:** Not applicable.

**Informed Consent Statement:** Not applicable.

**Data Availability Statement:** Data are contained within the article.

**Conflicts of Interest:** The authors declare that they have no known competing financial interests or personal relationships that could have appeared to influence the work reported in this paper.

## References

1. Liu, J.; He, C.; Zhang, M.; Yan, A. A systematic study of the microstructure, phase formation and magnetocaloric properties in off-stoichiometric La-Fe-Si alloys. *Acta Mater.* **2016**, *118*, 44–53. [CrossRef]
2. Franco, V.; Blázquez, J.; Ipus, J.; Law, J.; Moreno-Ramírez, L.; Conde, A. Magnetocaloric effect: From materials research to refrigeration devices. *Prog. Mater. Sci.* **2018**, *93*, 112–232. [CrossRef]
3. Li, L.; Yan, M. Recent progresses in exploring the rare earth based intermetallic compounds for cryogenic magnetic refrigeration. *J. Alloys Compd.* **2020**, *823*, 153810. [CrossRef]
4. Choe, W.; Pecharsky, V.K.; Pecharsky, A.O.; Gschneidner, K.A.; Young, V.G.; Miller, G.J. Making and breaking covalent bonds across the magnetic transition in the giant magnetocaloric material $Gd_5(Si_2Ge_2)$. *Phys. Rev. Lett.* **2000**, *84*, 4617–4620. [CrossRef] [PubMed]
5. Palstra, T.; Mydosh, J.; Nieuwenhuys, G.; van der Kraan, A.; Buschow, K. Study of the critical behaviour of the magnetization and electrical resistivity in cubic $La(Fe, Si)_{13}$ compounds. *J. Magn. Magn. Mater.* **1983**, *36*, 290–296. [CrossRef]
6. Thanh, D.T.C.; Brück, E.; Tegus, O.; Klaasse, J.C.P.; Gortenmulder, T.J.; Buschow, K.H.J. Magnetocaloric effect in MnFe(P,Si,Ge) compounds. *J. Appl. Phys.* **2006**, *99*, 08Q107. [CrossRef]
7. Shao, Y.; Lu, B.; Zhang, M.; Liu, J. An X-ray absorption spectroscopy study of La-Fe-Si-(H) magnetocaloric alloys. *Acta Mater.* **2018**, *150*, 206–212. [CrossRef]

8. Tang, W.H.; Liang, J.K.; Rao, G.H.; Yan, X.H. Study of AC susceptibility on the $LaFe_{13-x}Si_x$ system. *Phys. Status Solidi (A)* **1994**, *141*, 217–222. [CrossRef]
9. Wu, Q.; Sun, N.; Wang, X.; Li, L. Microstructure, magnetic properties and thermal conductivity of $LaFe_{11.2}Si_{1.8}$/Ta magnetocaloric composites. *J. Magn. Magn. Mater.* **2019**, *476*, 24–28. [CrossRef]
10. Fujita, A.; Akamatsu, Y.; Fukamichi, K. Itinerant electron metamagnetic transition in $La(Fe_xSi_{1-x})_{13}$ intermetallic compounds. *J. Appl. Phys.* **1999**, *85*, 4756–4758. [CrossRef]
11. Pecharsky, V.K.; Gschneidner, J.K.A. Giant magnetocaloric effect in $Gd_5(Si_2Ge_2)$. *Phys. Rev. Lett.* **1997**, *78*, 4494–4497. [CrossRef]
12. Fujieda, S.; Fukamichi, K.; Suzuki, S. Suppression of aqueous corrosion of $La(Fe_{0.88}Si_{0.12})_{13}$ by reducing dissolved oxygen concentration for high-performance magnetic refrigeration. *J. Alloys Compd.* **2014**, *600*, 67–70. [CrossRef]
13. Russek, S.L.; Zimm, C.B. Potential for cost effective magnetocaloric air conditioning systems. *Int. J. Refrig.* **2006**, *29*, 1366–1373. [CrossRef]
14. Hu, J.; Zhang, X.; Liu, H.; Fu, B.; Dong, Z.; Wang, Y. Microstructure, Corrosion Resistance, and Magnetic Properties of $LaFe_{12.35\text{-}x}Co_{0.65}Si_xC_{0.15}$ ($x$ = 1.3, 1.4, 1.5) Compounds after Corrosion in Distilled Water. *J. Supercond. Nov. Magn.* **2022**, *35*, 1569–1574. [CrossRef]
15. Zhang, E.Y.; Chen, Y.G.; Tang, Y.B. Investigation on corrosion and galvanic corrosion in $LaFe_{11.6}Si_{1.4}$ alloy. *Mater. Chem. Phys.* **2011**, *127*, 1–6. [CrossRef]
16. Xue, J.N.; Long, Y.; Wang, Y.; Hu, J.; Zong, S.T. Corrosion behavior and phase formation of $LaFe_{13-x}Si_xB_y$ alloys. *Mater. Des.* **2017**, *129*, 1–8. [CrossRef]
17. Hu, J.; Guan, L.; Fu, S.; Sun, Y.; Long, Y. Corrosion and latent heat in thermal cycles for $La(Fe,Mn,Si)_{13}$ magnetocaloric compounds. *J. Magn. Magn. Mater.* **2014**, *354*, 336–339. [CrossRef]
18. Hu, J.; Dong, Z.Q.; Shen, Y.M.; Fu, B.; Zhang, B.F. Effect of excess lanthanum on corrosion and magnetocaloric property of $LaFe_{11.5}Si_{1.5}$ compounds. *J. Rare Earths* **2019**, *37*, 110–114. [CrossRef]
19. Zhang, M.; Sun, W.; Long, Y.; Qin, C.; Ye, R.C. Effect of chromium on magnetic properties and corrosion resistance of $LaFe_{11.5}Si_{1.5}$ compound. *J. Rare Earths* **2013**, *31*, 4. [CrossRef]
20. Sun, N.; Zhao, X.; Song, Y.; Liu, R.; Zhang, Z. Electroless plating Ni-P coatings on $La(Fe, Si)_{13}$ hydride bulks for room-temperature magnetic-refrigeration application. *J. Magn. Magn. Mater.* **2021**, *525*, 167685. [CrossRef]
21. Zhang, E.Y.; Chen, Y.; Tang, Y. Effect of copper ion implantation on corrosion morphology and corrosion behavior of $LaFe_{11.6}Si_{1.4}$ alloy. *J. Rare Earths* **2012**, *30*, 269–273. [CrossRef]
22. Xiang, M.; Li, T.; Zhao, Y.; Chen, M. The Influence of Negative Voltage on Corrosion Behavior of Ceramic Coatings Prepared by MAO Treatment on Steel. *Coatings* **2022**, *12*, 710. [CrossRef]
23. Liu, C.; Liu, P.; Huang, Z.; Yan, Q.; Guo, R.; Li, D.; Jiang, G.; Shen, D. The correlation between the coating structure and the corrosion behavior of the plasma electrolytic oxidation coating on aluminum. *Surf. Coat. Technol.* **2016**, *286*, 223–230. [CrossRef]
24. Malinovschi, V.; Marin, A.; Moga, S.; Negrea, D. Preparation and characterization of anticorrosive layers deposited by micro-arc oxidation on low carbon steel. *Surf. Coat. Technol.* **2014**, *253*, 194–198. [CrossRef]
25. Kloprogge, J.T.; Duong, L.V.; Wood, B.J.; Frost, R.L. XPS study of the major minerals in bauxite: Gibbsite, bayerite and (pseudo-)boehmite. *J. Colloid Interface Sci.* **2006**, *296*, 572–576. [CrossRef] [PubMed]
26. Wang, Y.; Jiang, Z.; Yao, Z. Preparation and properties of ceramic coating on Q235 carbon steel by plasma electrolytic oxidation. *Curr. Appl. Phys.* **2009**, *9*, 1067–1071. [CrossRef]
27. Hirschorn, B.; Orazem, M.E.; Tribollet, B.; Vivier, V.; Frateur, I.; Musiani, M. Determination of effective capacitance and film thickness from constant-phase-element parameters. *Electrochim. Acta* **2010**, *55*, 6218–6227. [CrossRef]
28. Wang, Y.; Jiang, Z.; Yao, Z.; Tang, H. Microstructure and corrosion resistance of ceramic coating on carbon steel prepared by plasma electrolytic oxidation. *Surf. Coat. Technol.* **2010**, *204*, 1685–1688. [CrossRef]
29. Lopez, S.G.R.; Torres, A.J.; Torres, B.; Rams, J. 316L stainless steel coatings on ZE41 magnesium alloy using HVOF thermal spray for corrosion protection. *Surf. Coat. Technol.* **2016**, *287*, 9–19. [CrossRef]
30. Fei, C.; Hai, Z.; Chen, C.; Xia, Y. Study on the tribological performance of ceramic coatings on titanium alloy surfaces obtained through microarc oxidation. *Prog. Org. Coat.* **2009**, *64*, 264–267. [CrossRef]
31. Li, Q.; Liang, J.; Wang, Q. Plasma Electrolytic Oxidation Coatings on Lightweight Metals. In *Modern Surface Engineering Treatments*; BoD—Books on Demand: Norderstedt, Germany, 2013; pp. 75–99.
32. Pan, Y.; Wang, D.; Chen, C. Effect of negative voltage on the microstructure, degradability and in vitro bioactivity of microarc oxidized coatings on ZK60 magnesium alloy. *Mater. Lett.* **2014**, *119*, 127–130. [CrossRef]
33. Yang, W.; Li, Q.; Liu, C.; Liang, J.; Peng, Z.; Liu, B. A comparative study of characterisation of plasma electrolytic oxidation coatings on carbon steel prepared from aluminate and silicate electrolytes. *Surf. Eng.* **2017**, *34*, 54–62. [CrossRef]
34. Li, T.; Chen, G.; Xiang, M.; Zhao, Y.; Chen, M. Effect of $ZrSiO_4$ Concentration on the Microstructure and Corrosion Resistance of MAO Coatings Formed on AZ91 Magnesium Alloy. *Front. Mater.* **2022**, *8*, 799780. [CrossRef]
35. Bin, F.; Yi, L.; Pu-Ji, S.; Tao, M.; Bo, B.; A-Ru, Y.; Ren-Jie, C. Hydrogen absorption of LaFe 11.5 Si 1.5 compound under low hydrogen gas pressure. *Chin. Phys. B* **2009**, *18*, 4506–4510. [CrossRef]
36. Ouyang, Y.; Zhang, M.; Yan, A.; Wang, W.; Guillou, F.; Liu, J. Plastically deformed La–Fe–Si: Microstructural evolution, magnetocaloric effect and anisotropic thermal conductivity. *Acta Mater.* **2020**, *187*, 1–11. [CrossRef]

37. Liu, J.; Krautz, M.; Skokov, K.; Woodcock, T.G.; Gutfleisch, O. Systematic study of the microstructure, entropy change and adiabatic temperature change in optimized La-Fe-Si alloys. *Acta Mater.* **2011**, *59*, 3602–3611. [CrossRef]
38. Ma, T.; Long, Y.; Bao, B.; Fu, B.; Wang, X.Q.; Jin, F.L. Influence of Demagnetizing Effects on Entropy Change of Magnetocaloric Materials under Low Magnetic Fields. *J. Rare Met.* **2010**, *7*, 103–109. [CrossRef]